



Vessel enhancement filter using directional filter bank

Phan T.H. Truc^a, Md. A.U. Khan^b, Young-Koo Lee^{a,*}, Sungyoung Lee^a, Tae-Seong Kim^c

^a Department of Computer Engineering, Kyung Hee University, 1 Seocheon-dong, Giheung-gu, Yongin-si, Gyeonggi 449-701, South Korea

^b Comsats Institute of Information Technology, Abbottabad, Pakistan

^c Department of Biomedical Engineering, Kyung Hee University, South Korea

ARTICLE INFO

Article history:

Received 5 March 2007

Accepted 21 July 2008

Available online 3 August 2008

Keywords:

Vessel enhancement filter

Directional filter bank

Medical imaging

Angiography images

ABSTRACT

Vessel enhancement is an important preprocessing step in accurate vessel-tree reconstruction which is necessary in many medical imaging applications. Conventional vessel enhancement approaches used in the literature are Hessian-based filters, which are found to be sensitive to noise and sometimes give discontinued vessels due to junction suppression. In this paper, we propose a novel framework for vessel enhancement for angiography images. The proposed approach incorporates the use of line-like directional features present in an image, extracted by a directional filter bank, to obtain more precise Hessian analysis in noisy environment and thus can correctly reveal small and thin vessels. Also, the directional image decomposition helps to avoid junction suppression, which in turn, yields continuous vessel tree. Qualitative and quantitative evaluations performed on both synthetic and real angiography images show that the proposed filter generates better performance in comparison against two Hessian-based approaches. In average, it is relatively 3.74% and 7.02% less noise-sensitive and performs 5.83% and 6.21% better compared to the two approaches, respectively.

© 2008 Elsevier Inc. All rights reserved.

1. Introduction

Correct assessment, especially accurate visualization and quantification, of blood vessels reflected in X-ray angiograms or angiography images plays a significant role in a number of clinical procedures. For various medical diagnostic tasks, it is necessary to measure vessel width, reflectivity, tortuosity, and abnormal branching. For example, detecting the occurrence of vessels of a certain width may reveal the signs of stenoses. Grading of stenoses is of importance to diagnose the severity of vascular disease and then to determine the treatment therapy [1,2]. Moreover, planning and performing neurosurgical procedures require an exact insight into blood vessels and their branches, which exhibit much variability. In planning, they provide information on where the blood is drawn and drained to differentiate between the feeding vessel and the transgressing vessel. While transgressing vessels need to be preserved, feeding ones are selectively closed through the artery in interventional neuroradiology such as brain arteriovenous malformations treatment. During surgery the vessels serve to provide landmarks and guidelines to the lesion. In short, the accuracy in navigation and localization of clinical procedures is determined by how minute and subtle the vascular information is. Although it is possible for medical experts to delineate vessels, manual delin-

eation of the vasculature becomes tedious or even impossible when the number of vessels in an image is large or when a large number of images is acquired. Therefore, the development of automatic and accurate vessel-tree reconstruction from angiograms is highly desirable. Unfortunately, it has proven to be a challenging task. The key fact is that vessels cannot be characterized uniformly. Because the blood either by itself or by the contrast agent it carries is responsible for the vessel contrast to the background, large vessels usually have high contrast while small ones resemble the background (see Fig. 1a). Non-uniform illumination as shown in Fig. 1b, which is one of the major sources of angiography image degradation [3], is also a hindrance for accurate reconstruction because it is likely to make an individual vessel broken into several segments. According to [4,5], current automatic computer-assisted procedures are still far from providing a precise spatial representation of the vessel tree.

In order to achieve an accurate vessel-tree reconstruction, the vessel enhancement procedure, which is the main issue of this paper, is an important preprocessing step. There are a variety of vessel enhancement methods in the literature. Some works have taken linear filtering approach. Poli and Valli [6] proposed a computationally efficient algorithm based on a set of linear filters, obtained as linear combinations of properly shifted Gaussian kernels, sensitive to vessels of different orientation and radius. Another type of linear filters, the morphological connected-set filter, was utilized by Wilkinson and Westenberg [7] to capture filamentous structures. Together with a shape criterion that can distinguish

* Corresponding author. Fax: +82 31 202 2520.

E-mail address: yklee@khu.ac.kr (Y.-K. Lee).

URL: <http://uclab.khu.ac.kr> (Y.-K. Lee).

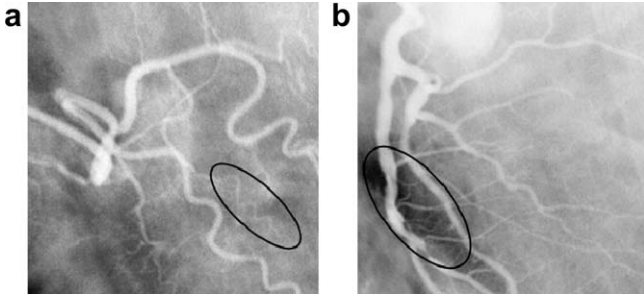


Fig. 1. Angiography images with typical hindrances for accurate vessel-tree reconstruction such as (a) low-contrast vessels and (b) non-uniform illumination.

filamentous structures from others, connected-set filters can help to extract filamentous details without distortion. Similarly, Eiho and Qian [8] and Zana and Klein [9] used morphological operators such as erosion, dilation, and Top-Hat to enhance the shape of the artery and remove other points. However, these methods were unable to suppress sudden noise and edge noise and were less efficient on capillaries. A different linear filtering approach which combined Laplacian filter with fuzzy logic was presented by Yan et al. [10]. Small vessels were not captured satisfactorily by this approach either.

Non-linear anisotropic filtering has also been applied to vessel enhancement [11–13]. This method searches for the local orientation of a vessel to perform anisotropic smoothing without blurring its edge. While Krissian et al. performed a particular version of anisotropic diffusion, Orkisz et al. used a kind of filter bank called “sticks”, which can be seen as a set of directional structuring elements. Similar approaches were also proposed by Czerwinski et al. [14,15], Kutka and Stier [16], Chen and Hale [17], and Du et al. [18,19]. The last two combined the outputs of directional operators without an explicit extraction of the vessel local orientation. The main disadvantage of the methods in this category is that they can hardly detect vessels in a wide range due to the fixed scale analysis. Although they can be extended to multiple scales by using sticks of variable length, the computation time would increase very much.

Hessian-based multiscale filtering has been proposed in a number of vessel enhancement approaches [20–25]. One advantage of the approaches in this category is that vessels in a large range of diameters can be captured due to the multiscale analysis. In these methods, an input image is first convolved with the derivatives of a Gaussian at multiple scales and then the Hessian matrix is analyzed at each pixel in the resulting image to determine the local shape of the structures at that pixel (see Fig. 2a). The ratio between the minimum and the maximum Hessian eigenvalues is small for line-like structures but it should be high for blob-like ones. Specifically, Krissian et al. [26] introduced several models of vessels and used the Hessian eigenvalues to define a set of candidate pixels

which could be the centerlines of vessels. At each of these candidates, pre-defined multiscale response functions were computed to determine the likelihood of the pixel corresponding to vessels of different scales (radii). The drawbacks of the Hessian-based approaches are that they are highly sensitive to noise due to the second-order derivatives and that they tend to suppress junctions since junctions are characterized same as the blob-like structures. Junction suppression leads to the discontinuity of the vessel network, which is of course undesirable. To deal with this problem, Agam et al. [27] proposed a filter model which is based on the correlation matrix of the regularized gradient vectors (first-order derivatives), to avoid the need for second-order derivatives as demonstrated in Fig. 2b. This model generated good performance when dealing with thoracic CT images. However, when dealing with angiography images, which are more noisy and suffer from the non-uniform illumination, it shares the same limitations of Hessian-based filters in finding small and low-contrast vessels. The reason is that it is still using the Hessian eigenvalues to pre-select the vessel-candidate pixels at which the filter is applied.

In this paper, we propose a new framework for the vessel enhancement filter utilizing the directional information present in an image. This study focuses on the processing of 2D images such as X-ray angiography and retinal photography images. In such applications as intervention planning, blood vessel and retinal pathology, blood-flow analysis, or drug evaluation, 2D imaging is often the method of choice since it provides sufficiently good results although 3D imaging techniques would provide more information. The proposed approach alleviates the calculation of the Hessian eigenvalues in noisy environment. Specifically, the input image is first decomposed by a *decimation-free directional filter bank* (DDFB) into a set of directional images, each of which contains line-like features in a narrow directional range. The directional decomposition has two advantages. One is, noise in each directional image will be significantly reduced compared to that in the original one due to its omni-directional nature. The other is, because one-directional image contains only vessels with similar directions, the Hessian eigenvalue calculation in it is facilitated. Then, distinct appropriate enhancement filters are applied to enhance vessels in the respective directional images. Finally, the enhanced directional images are recombined to generate the output image with enhanced vessels and suppressed noise. This decomposition–filtering–recombination scheme also helps to preserve junctions. The experimental results show that our approach is less noise-sensitive, can reveal small vessel network, and avoid junction suppression.

The paper is organized as follows. In Section 2, we introduce the DDFB and discuss about the mathematical model of vessels while Section 3 describes our approach in details. Experimental results on synthetic data sets and real angiography and retinal photography images are shown in Section 4. Finally, conclusion is made after some discussions in Section 5.

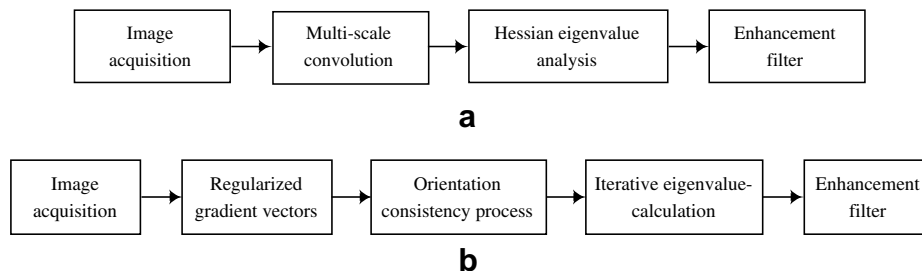


Fig. 2. Block diagrams of (a) conventional Hessian-based and (b) correlation-based approaches.

2. Methodology

In this section, we briefly describe the directional filter bank (DFB) and its adapted version, the DDFB which is used in our proposed framework. The mathematical background for a vessel model on which the enhancement filter is based is also introduced.

2.1. Directional filter bank

DFB was originally proposed by Bamberger and Smith [28]. It was shown that DFB can decompose the spectral region of an input image into $n = 2^k$ ($k = 1, 2, \dots$) wedge-shaped like passbands which correspond to linear features in a specific direction in spatial domain. Initially, DFB was designed to provide image compression [29]. Later on in [30,31], it was used in collaboration with directional energy for image enhancement purpose. Recently, in [32],

DFB and directional energy were tuned to provide fingerprint recognition.

Outputs of DFB were named as subbands. One major drawback of original DFB proposed in [28] is that subbands become visually distorted due to aliasing. One possible solution was provided by Park et al. [33], where it was pointed out that aliasing was produced due to non-diagonalization of overall downsampling matrix. Then the authors proposed in [34] a new DFB structure as follows.

2.1.1. First stage of DFB

Construction of the first stage of DFB requires a pair of diamond-shaped like passband filters, $H_0(\omega_1, \omega_2)$ and $H_1(\omega_1, \omega_2)$, a modulator, and a Quincunx downsampling matrix as shown in Fig. 3a, where $\vec{\omega} = (\omega_1, \omega_2)^T$ is a pair of 2D Fourier frequency variables. Modulator used in this stage shifts frequency spectrum of an input image by π in any of the two directions. In this structure, Q is

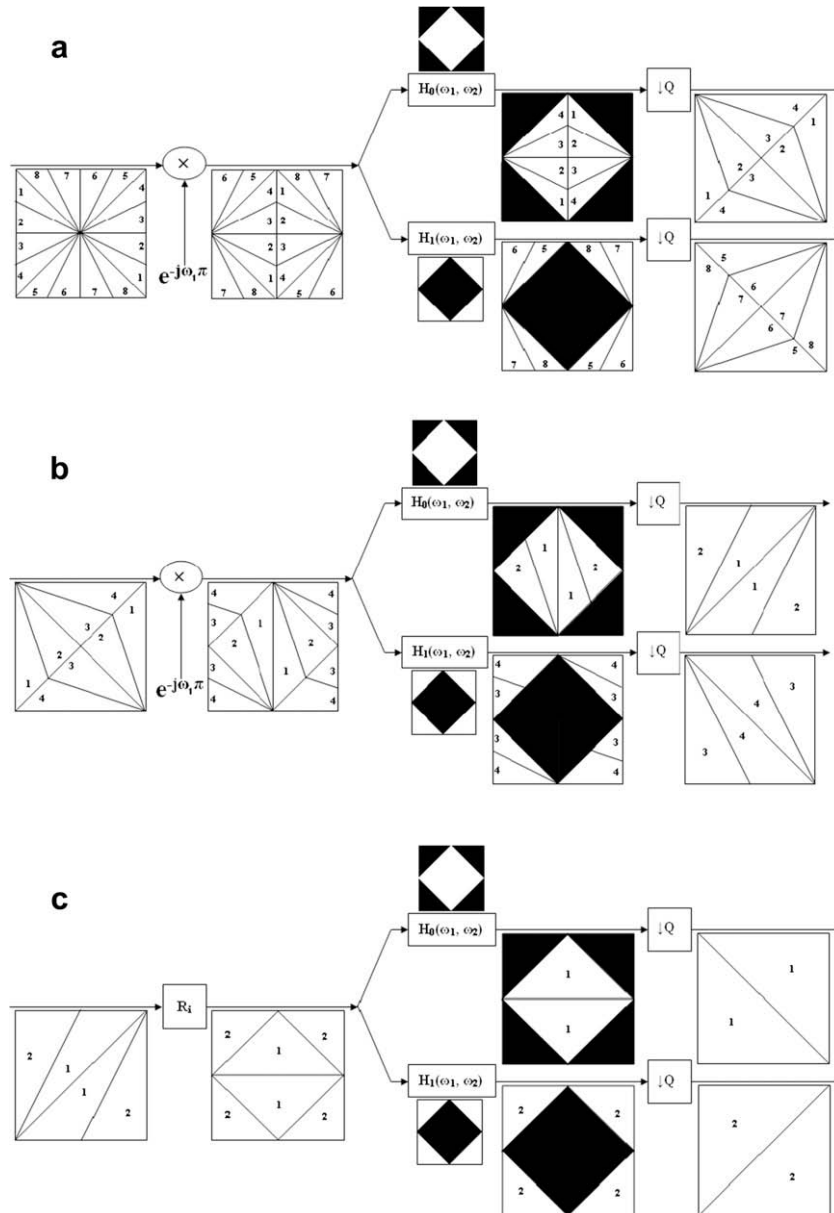


Fig. 3. The DFB structure in [34]. (a) First stage, (b) second stage, and (c) third stage. Subbands produced by the first stage are used as input to the second stage and so on. The size of subbands is smaller than that of the original image, which is good for image compression but causes problems for image analysis.

a Quincunx non-separable downsampling 2×2 matrix which not only downsamples but also rotates the image at an angle of 45° .

2.1.2. Second stage of DFB

Requirements for construction of the second stage of DFB are same as those for the first one. Subbands produced by the first stage are used as input to the second stage. Fig. 3b shows the spectral geometry of subbands created by the second stage. It is evident that these subbands have a parallelogram-shaped geometry.

2.1.3. Third stage of DFB

The additional requirements for construction of the third stage (see Fig. 3c) as compare to the first and second are resampling matrices and post-sampling matrices. Resampling matrices R_i are used to map parallelogram-shaped passbands to diamond-shaped passbands and post-sampling matrices to convert the overall non-diagonal sampling matrix to the diagonal one.

2.2. Decimation-free directional filter bank

Another disadvantage of DFB is that the subbands are smaller in size as compare to the original image. The reduction in size is due to the presence of decimators. As far as image compression is concerned, decimation is a must condition. However, when DFB is employed for image analysis purposes, decimation causes two problems. One is, as we increase the directional resolution, spatial resolution starts to decrease [35], due to which we loose the correspondence among the pixels of DFB outputs. The other is, an extra process of interpolation is involved prior to enhancement or recognition computation [31,36,32]. This extra interpolation process not only affects the efficiency of whole system but also produces false artifacts which can be harmful especially in case of medical imagery. Some vessels may be broken and some can be falsely connected to some other vessels due to the artifacts produced by interpolation. So a need arises to modify directional filter bank structure in a sense that no decimation is required during analysis section. To meet that need, the authors in [37,33] presented new rules to modify DFB. Based on those rules, we suggest to shift the decimators and resamplers to the right of the filters to make a *decimation-free directional filter bank* (DDFB), which yields directional images rather than directional subbands. This consequently results in elimination of interpolation and naturally fits the purposes of feature analysis. The block diagram of DDFB structure is shown in Fig. 4.

2.2.1. First stage of DDFB

Construction of the first stage of DDFB only requires two filters which are $H_{00}(\omega_1, \omega_2)$ and $H_{11}(\omega_1, \omega_2)$. They have hourglass-shaped like passbands as shown in Fig. 4a. Hourglass-shaped filters are created by shifting the modulators present at the first stage of DFB to the left of filters using rules proposed in [31]. So the interrelation between filters used during the first stage of DFB and that of DDFB can be given as

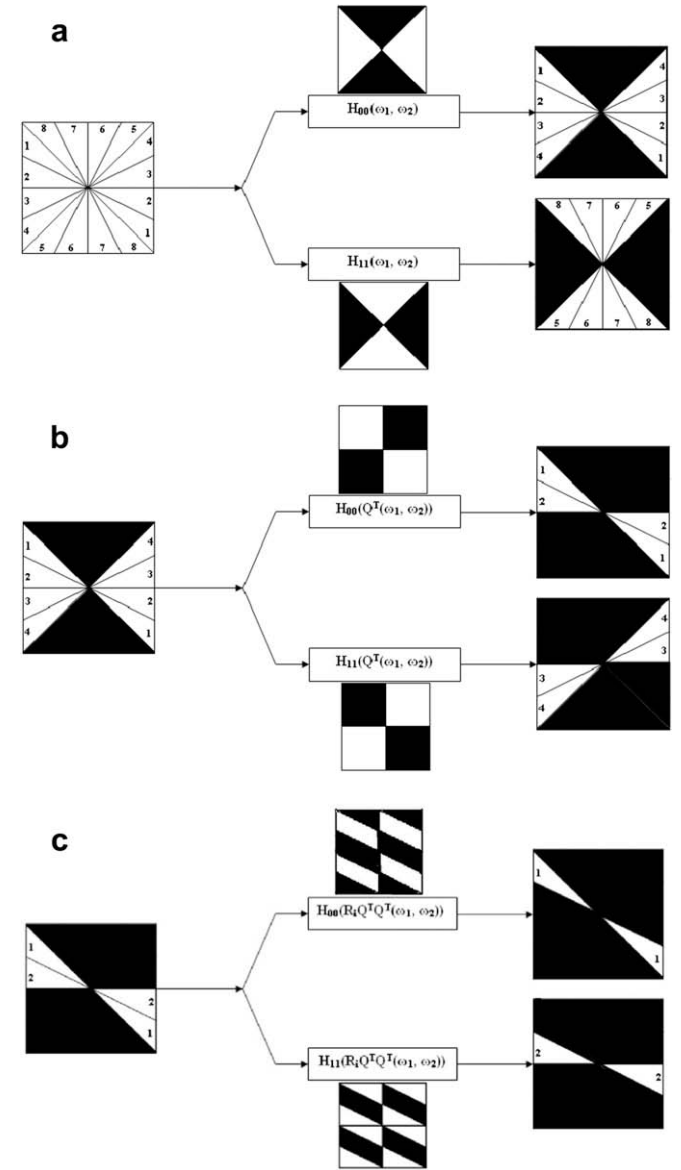


Fig. 4. DDFB structure. (a) First stage, (b) second stage, and (c) third stage. DDFB provides directional images of same size as the original image, which fits the purposes of image analysis.

$$H_{00}(\omega_1, \omega_2) = H_0(\omega_1 + \pi, \omega_2), \quad (1)$$

$$H_{11}(\omega_1, \omega_2) = H_0(\omega_1, \omega_2 + \pi), \quad (2)$$

where $H_0(\omega_1, \omega_2)$ is a diamond-shaped passband filter used during the first stage of DFB. No downsampler is applied after the input image is filtered by $H_{00}(\omega_1, \omega_2)$ and $H_{11}(\omega_1, \omega_2)$. By doing so, the size of outputs from the first stage becomes equal to the size of input

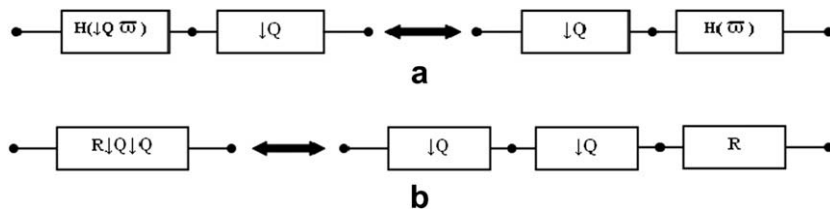


Fig. 5. Rules used in this paper to shift resampling and downsampling matrix to right.

image. Due to this reason, these outputs are named as *directional images*.

2.2.2. Second stage of DDFB

The filters required for the construction of the second stage are $H_{00}(Q^T(\omega_1, \omega_2))$ and $H_{11}(Q^T(\omega_1, \omega_2))$, where T represents transpose and Q is same as the Quincunx downsampling matrix in the first stage of DFB. Basically the Q, which should have been in the first stage of DDFB, was shifted to the right of the second stage filter using Fig. 5. Filters of this stage of DDFB can be related to filters of that of DFB by the following equations:

$$H_{00}(Q^T(\omega_1, \omega_2)) = H_0(Q^T(\omega_1 + \pi, \omega_2)), \quad (3)$$

$$H_{11}(Q^T(\omega_1, \omega_2)) = H_0(Q^T(\omega_1, \omega_2 + \pi)). \quad (4)$$

Directional images obtained from the first stage of DDFB are filtered through these two filters. No further operation is required at the end of this stage. Spectral regions of directional images obtained after filtering through this stage's filters are shown in Fig. 4b.

2.2.3. Third stage of DDFB

Filters used during the third stage of DDFB are $H_{00}^i(\omega_1, \omega_2)$ and $H_{11}^i(\omega_1, \omega_2)$, where $i = 1, 2, 3$, and 4 as shown in Fig. 4c. Overall eight different filters are created to be used during this stage. Mathematically this stage of DDFB can be related to that of DFB as

$$H_{00}^i(\omega_1, \omega_2) = H_0(R_i^T Q^T Q^T(\omega_1 + \pi, \omega_2)), \quad (5)$$

$$H_{11}^i(\omega_1, \omega_2) = H_0(R_i^T Q^T Q^T(\omega_1, \omega_2 + \pi)), \quad (6)$$

where R_i and Q are, respectively, the same resampling and downsampling matrices as used in DFB.

Basically, we have shifted all the modulators, the downsamplers and resampling matrices present in DFB to the right of all the filters. So, at the end of the third stage we will be left with two downsampling matrices, one resampling matrix followed by the post-sampling matrix. We do not apply these matrices onto our directional images. Directional images present at the third stage of DDFB are visually correct as no downsampling was applied to input image during the whole structure of DDFB. Fig. 6 demonstrates eight-directional images obtained by applying DDFB on the original image shown in Fig. 1b with $n = 8$ (i.e., $k = 3$).

Although we described eight-band DDFB, it can be extended to 16-band and 32-band DDFB and so on. For this extension to take place, we can take advantage of simple extension rules for DFB as described in [38]. For a given application, to decide how many directional images are needed, we assess how much directional resolution we are in need of, at the cost of additional computation. In our angiogram enhancement, we found 16-directional decomposition a good compromise between directional resolution and computational cost.

Furthermore, the 2D DDFB can be extended to 3D DDFB on the same lines as 2D DFB being converted to 3D DFB as an optimum three-dimensional matched filter for linearly moving objects in noise. More details can be found in [38] where the 3D DFB is referred to as velocity selective filter bank (VSFB) for emulating the behavior of the spatio-temporal continuous wavelet transform (CWT) that has proven useful for motion estimation [39,40]. The VSFB approach offers a computational advantage over direct implementation of the CWT in the sense that it exploits the temporal information in addition to 2D spatial coordinates which is critical in some real world applications.

2.3. A comparative analysis between DDFB and DFB

We have avoided the aliasing present in DFB by shifting of resampling and downsampling matrices to the right. Doing so we

are able to get directional images of the same size as the original image. One of the main advantages of DDFB is that due to absence of aliasing, directional images are visually correct.

In previously proposed DFB, spatial resolution decreases at least as fast as the directional resolution increases. The more one knows about the orientation of a feature, the less he knows about its length and vice versa [35]. However, in DDFB, there is no interdependency between the length and orientation of the feature. This means that increasing directional resolution does not affect spatial resolution. Although in DDFB no downsamplers are employed at all, complexity will be higher due to the increased data size. Nevertheless, artifacts due to aliasing are avoided in reconstruction. This is important in medical images as some aliasing artifacts can be misleading.

In DDFB, since directional images are of same size as the original image, no interpolation step to establish one-to-one pixel cor-

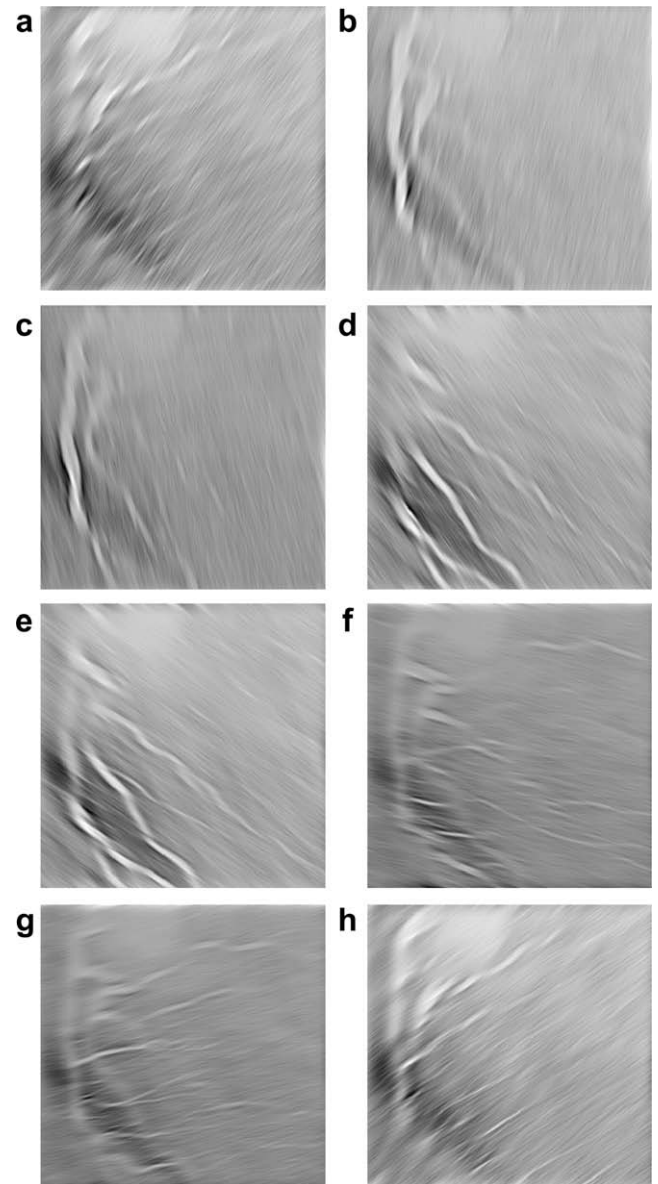


Fig. 6. Eight-directional images of the angiography image shown in Fig. 1b after applying DDFB with $n = 8$. (a) Corresponds to orientations in the range 45–67.5°, (b) 67.5–90°, (c) 90–112.5°, (d) 112.5–135°, (e) 135–157.5°, (f) 157.5–180°, (g) 0–22.5°, and (h) 22.5–45°.

respondence is needed like in DFB. As a result, DDFB avoids false artifacts produced during interpolation in subbands.

The synthesis section of DFB requires exactly the reverse process of the analysis section. In contrast, at any stage in DDFB, synthesis can be achieved by the simple addition of directional images. So the overall process of synthesis section is simplified in DDFB.

2.4. Vessel model

An intensity image $I(p)$, where $p = (x, y)$, can be approximated by its Taylor expansion about a point p_0 up to the second order

$$I(p) \simeq I(p_0) + \Delta p^T \cdot \nabla I(p_0) + \frac{1}{2} \Delta p^T H(I(p_0)) \Delta p, \quad (7)$$

$$\Delta p = p - p_0, \quad (8)$$

where $\nabla I(p_0)$ and $H(I(p_0))$ are, respectively, the gradient vector and the Hessian matrix at point p_0 .

Without loss of generality, we assume that in 2D X-ray angiography images, vessels are bright over the dark background and the brightness is decreased from their centers toward their boundaries. Therefore, a vessel is modeled as a tube with a Gaussian profile across its axis, which is identical to the x -axis

$$I_0(x, y) = \frac{C}{2\pi\sigma_0^2} e^{-\frac{y^2}{2\sigma_0^2}}. \quad (9)$$

In Hessian-based vessel enhancement approaches, a vessel is declared when the ratio between the minimum and maximum Hessian eigenvalues is low. Its direction is considered to be the eigenvector corresponding to the smallest eigenvalue in absolute value.

The Hessian of the above model can be expressed as

$$H = \begin{bmatrix} \frac{\partial^2 I_0}{\partial x^2} & \frac{\partial^2 I_0}{\partial x \partial y} \\ \frac{\partial^2 I_0}{\partial x \partial y} & \frac{\partial^2 I_0}{\partial y^2} \end{bmatrix} = \begin{bmatrix} 0 & 0 \\ 0 & \frac{y^2 - \sigma_0^2}{\sigma_0^4} I_0 \end{bmatrix} \quad (10)$$

and its eigenvalues and eigenvectors

$$\lambda_1 = 0; \quad \lambda_2 = \frac{y^2 - \sigma_0^2}{\sigma_0^4} I_0, \quad (11)$$

$$\vec{v}_1 = (1, 0); \quad \vec{v}_2 = (0, 1).$$

In order to capture vessels with various sizes, one should compute the gradient and the Hessian at multiple scales σ in a certain range. In this case, the only way to ensure the well-posed properties, such as linearity, translation invariance, rotation invariance, and re-scaling invariance, is the use of linear scale space theory [41,42], in which differentiation is calculated by a convolution with derivatives of a Gaussian

$$I_x = \sigma^\gamma G_{x,\sigma} * I; \quad I_y = \sigma^\gamma G_{y,\sigma} * I, \quad (12)$$

where I_x and I_y are, respectively, the spatial derivatives in x - and y -direction of the image $I(x, y)$ and $G_{x,\sigma}$ and $G_{y,\sigma}$ spatial derivatives of a Gaussian with standard deviation σ

$$G_\sigma(x, y) = \frac{1}{2\pi\sigma^2} e^{-\frac{x^2+y^2}{2\sigma^2}}. \quad (13)$$

The parameter γ was proposed by Lindeberg [42,43] to normalize the derivatives of the image. This normalization is necessary for comparison of the response of differentiations at multiple scales because the intensity and its derivatives are decreasing functions of scale. In vessel enhancement application, where no scale is preferred, γ is usually set to one.

When applying the multiscale analysis, the model in (9) is convolved with a Gaussian of standard deviation σ . The derivations in (10) and (11) are still correct except that σ_0 is replaced with

$\sqrt{\sigma_0^2 + \sigma^2}$. We can see from those derivations that at pixels inside the vessel ($y^2 < \sigma_0^2$), we have one negative eigenvalue corresponding to the eigenvector orthogonal to the axis of the vessel. The other eigenvalue, which is smaller in absolute value, associates with the eigenvector having the same direction as the vessel axis. Note also that in this case, when the vessel direction (\vec{v}_1) is aligned with the x -axis, the eigenvalues of Hessian are same as its diagonal values. This fact has been exploited in our work to compute the Hessian eigenvalues with less noise sensitiveness compared to the normal way. Details of the proposed approach, named as *DFB-based vessel enhancement filter*, are described as follows.

3. DFB-based vessel enhancement filter

The proposed method consists of three steps, as shown in Fig. 7: Step 1: construction of directional images, Step 2: vessel enhancement, and Step 3: recombination of enhanced directional images.

3.1. Construction of directional images

An angiography image, in which vessels can be modeled as piece-wise line-like segments, could be an appropriate candidate

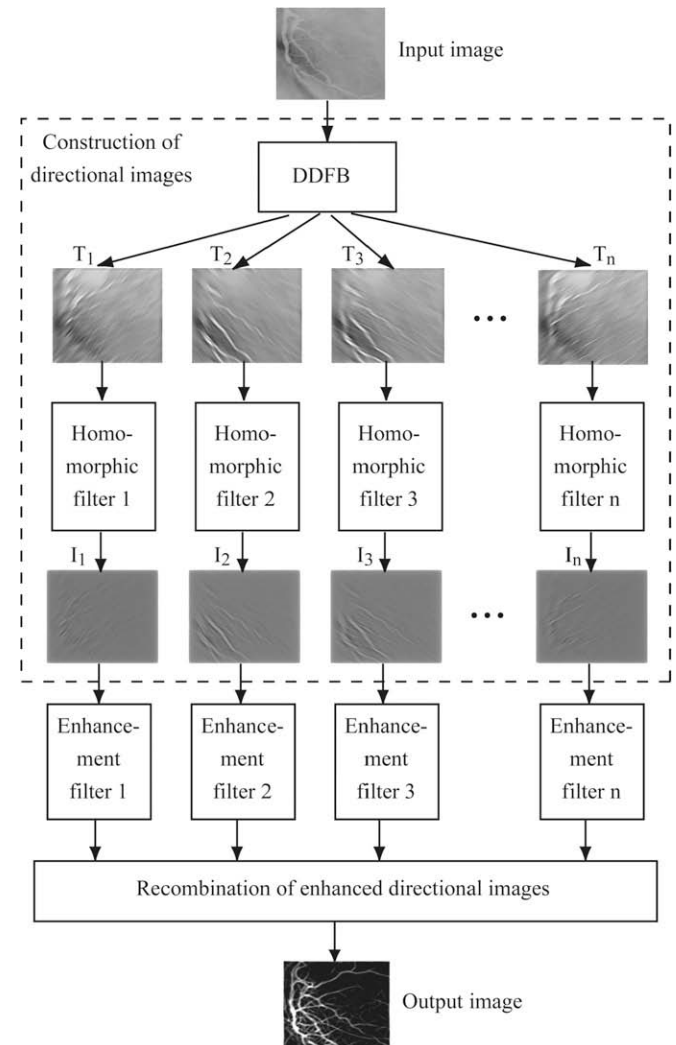


Fig. 7. Block diagram of the proposed enhancement framework. There are three main steps: construction of directional images, vessel enhancement, and recombination of enhanced directional images.

for the decomposition using DDFB. Specifically, the input image is decomposed to $n = 2^k$ ($k = 1, 2, \dots$) directional images T_i . The motivation here is to detect thin and low-contrast vessels (which are largely directional in nature) while avoiding false detection of non-vascular structures. Directional segregation property of DDFB is helpful in eliminating randomly oriented noise patterns and non-vascular structures which normally yield similar amplitudes in all directional images (see Fig. 6).

Before these directional images are enhanced in the next step, they are utilized to efficiently remove non-uniform illumination (NUI), which limits the correct vessel enhancement as introduced in Introduction. One conventional approach to correct NUI is to directly apply homomorphic filtering [44] on the original image. A general image can be characterized by two components: (1) the illumination component, which changes slowly in a neighborhood due to light source characteristics and thus is low-frequency and (2) the reflectance component, which is determined by the amount of light reflected by the objects and therefore is high-frequency. The homomorphic filter is to suppress the low-frequency component while enhance the high-frequency one. However, the direct application of homomorphic filtering is sometimes unsatisfactory because it may enhance high-frequency background noise as can be seen in Fig. 8a. Tuning the filter parameters in this case suffers from a compromise: the more NUI is removed, the more background noise is enhanced. Differently, we propose employing a homomorphic filter matched with its corresponding directional image as shown in the dash-boundary box in Fig. 7. This new arrangement provides us a better control on the parameters of individual homomorphic filter. For the sake of comparison, we show the recombination of directional homomorphic filtered images in Fig. 8b. The image is now largely uniformly illuminated without unexpected noise amplification.

3.2. Vessel enhancement

As pointed out in Section 2.4, in order to compute the Hessian eigenvalues with less noise sensitiveness, it is necessary to align the vessel direction with the x -axis. One possible way is to rotate the directional images. Nevertheless, image rotation requires interpolation which is likely to create artifacts and thus is harmful especially in case of medical imagery. We therefore rotate the coordinates rather than the directional images.

Suppose the directional image I_i ($i = 1, \dots, n$) corresponds to the orientations ranging from $\theta_{i,\min}$ to $\theta_{i,\max}$ (counterclockwise angle). Its associated coordinates Ox will be rotated to $Ox'y'$ by an amount as large as the mean value θ_i

$$\theta_i = \frac{\theta_{i,\min} + \theta_{i,\max}}{2}. \quad (14)$$

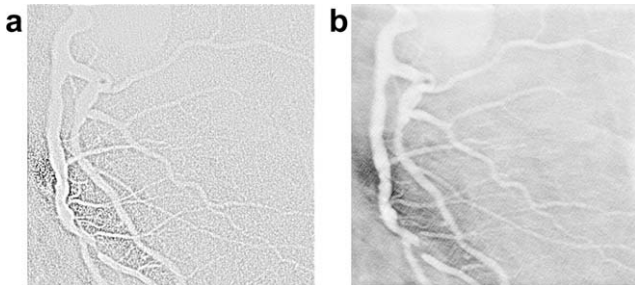


Fig. 8. Results of NUI removal for the image in Fig. 1b using homomorphic filter. (a) Direct filtering on the original image and (b) filtering on directional images and then recombining them. The former amplifies background noise whereas the latter does not.

According to (A-1)–(A-2) in the Appendix, Hessian matrix of the directional image I_i in the new coordinates $Ox'y'$ is determined as

$$H' \equiv \begin{bmatrix} h_{11} & h_{12} \\ h_{21} & h_{22} \end{bmatrix} = \begin{bmatrix} \frac{\partial^2 I_i}{\partial x'^2} & \frac{\partial^2 I_i}{\partial x' \partial y'} \\ \frac{\partial^2 I_i}{\partial x' \partial y'} & \frac{\partial^2 I_i}{\partial y'^2} \end{bmatrix}, \quad (15)$$

where

$$\frac{\partial^2 I_i}{\partial x'^2} = \frac{\partial^2 I_i}{\partial x^2} \cos^2 \theta_i + \frac{\partial^2 I_i}{\partial x \partial y} \sin(2\theta_i) + \frac{\partial^2 I_i}{\partial y^2} \sin^2 \theta_i, \quad (16)$$

$$\frac{\partial^2 I_i}{\partial y'^2} = \frac{\partial^2 I_i}{\partial x^2} \sin^2 \theta_i - \frac{\partial^2 I_i}{\partial x \partial y} \sin(2\theta_i) + \frac{\partial^2 I_i}{\partial y^2} \cos^2 \theta_i, \quad (17)$$

$$\frac{\partial^2 I_i}{\partial x' \partial y'} = -\frac{1}{2} \frac{\partial^2 I_i}{\partial x^2} \sin(2\theta_i) + \frac{\partial^2 I_i}{\partial x \partial y} \cos(2\theta_i) + \frac{1}{2} \frac{\partial^2 I_i}{\partial y^2} \sin(2\theta_i). \quad (18)$$

The Hessian eigenvalues are then defined by the diagonal values of H' . As proven in (9)–(11), these values are

$$h_{11} = 0 \text{ and } h_{22} = \frac{y'^2 - (\sigma_0^2 + \sigma^2)}{(\sigma_0^2 + \sigma^2)^2} I_0(x', y'), \quad (19)$$

where σ selected in a range S is the standard deviation of the Gaussian kernel used in the multiscale analysis.

Practically, the vessel axis is not, in general, identical to the x' -axis and so $h_{11} \approx 0$. Inside the vessel, $|y'| < \sqrt{\sigma_0^2 + \sigma^2}$ and thus h_{22} is negative. Therefore, vessel pixels are declared when $h_{22} < 0$ and $|\frac{h_{11}}{h_{22}}| \ll 1$.

To distinguish background pixels from others, we define a structureness measurement

$$C = \sqrt{h_{11}^2 + h_{22}^2}. \quad (20)$$

This structureness C should be low for background which has no structure and small derivative magnitude. Based on the above observations, the vessel filter output, which is similar to that in [20], can be defined as

$$\phi_\sigma(p) = \eta(h_{22}) \exp\left(-\frac{R^2}{2\beta^2}\right) \left[1 - \exp\left(-\frac{C^2}{2\gamma^2}\right)\right], \quad (21)$$

where $p = (x', y')$, $R = \frac{h_{11}}{h_{22}}$, β and γ are adjusting constants, and

$$\eta(z) = \begin{cases} 0 & \text{if } z \geq 0 \\ 1 & \text{if } z < 0. \end{cases} \quad (22)$$

The filter is analyzed at different scales σ in a range S . When the scale matches the size of the vessel, the filter response will be maximum. Therefore, the final vessel filter response is

$$\Phi(p) = \max_{\sigma \in S} \phi_\sigma(p). \quad (23)$$

One filter (23) is applied to one-directional image to enhance vessel structures in it.

3.3. Recombination of enhanced directional images

Each directional image now contains enhanced vessels in its directional range and is called the enhanced directional image.

Denote $\Phi_i(p)$, $i = 1, \dots, n$, as the enhanced directional images. As mentioned in Section 2.3, the synthesis of DDFB is achieved by simply summing all directional images. Thus, the output enhanced image $F(p)$ can be obtained by

$$F(p) = \frac{1}{n} \sum_{i=1}^n \Phi_i(p). \quad (24)$$

The whole filtering procedures can be summarized as follows. First, the input angiography image is decomposed into $n = 2^k$ ($k = 1, 2, \dots$)

directional images T_i using DDFB. Then, n distinct homomorphic filters are employed to n respective directional images to remove non-uniform illumination. The output uniformly illuminated directional images I_i are enhanced according to (21)–(23). Finally, all enhanced directional images are recombined to yield the final filtered image F as in (24).

4. Experimental results

In this section, experiments have been performed with both synthetic images and real angiography and retinal photography images to verify the performance of the proposed DFB-based enhancement filter in comparison with the filters introduced by Frangi et al. [20] and Shikata et al. [25], which are considered as the standard techniques. In experiments using our proposed filter, the input image is decomposed to 16-directional images ($n = 16$) as a trade-off between performance and computation time. If not stated otherwise, the scale range $S = \{1, \sqrt{2}, 2, 2\sqrt{2}, 4\}$ is used for all three models as proposed in [25]. The computation time (cpu time, in seconds), performed on an Intel Duo Core 1.86 GHz with 1 GB of RAM, will be given in each case.

4.1. Junction suppression

Fig. 9 shows the results of an synthetic image of size 158×176 which was processed by the three filter models. The synthetic image is designed to contain vessels of different sizes and junctions of different types. It is possible to see that the Frangi and Shikata filters suppress junctions while the DFB-based approach does not. The suppressed junctions make vessels discontinuous. Although this error may be small, it can cause the splitting of a single vessel, which in turn has a critical effect on the vessel-tree reconstruction accuracy.

It is the use of directional image decomposition that makes the proposed model work. Normally, a vessel has one principal direction, which is mathematically indicated by a small ratio between the minimum and maximum Hessian eigenvalue. Meanwhile, at a junction, where a vessel branches off, there are more than two principal directions, and thus the ratio of two eigenvalues is no longer small. As a result, the Frangi and Shikata filters consider those points as noise and then suppress them. The DFB-based ap-

proach, on the other hand, decomposes the input image to various directional images, each of which contains vessels with similar orientations. Consequently, junctions do not exist in directional images and so are not suppressed during the filtering process. After that, due to the recombination of enhanced directional images, junctions are re-constructed at those points which have vessel values in more than two-directional images. Therefore, junctions are not only preserved but also enhanced in the final output image.

4.2. Noise sensitivity

To compare the performances of the filters with respect to noise levels, we construct a set of phantom images as follows. First of all, one original phantom image with various typical hindrances for accurate vessel detection is created (see Fig. 10a) and later on used as the “ground truth”. In this 512×512 sized phantom, fifteen vessel segments are constructed for a wide range of widths and directions to model a vascular image. For the sake of description, these segments are numbered in an increasing order from left to right and top to bottom. Segment 1 represents distinct branch points in a real angiography image, and Segments 4 through 7 characterize junctions with different widths while Segment 3 stands for vessel orientation diversity. Moreover, Segments 2, 12, and 14 are designed deliberately to have variable cross-sectional widths. In addition, common challenges such as the presence of close parallel vessels (Segments 8, 9, and 11), very thin vessels (Segment 10), discontinued vessels (Segment 13), and vessels with variable intensities along their length (Segment 15) are also incorporated into the phantom. Next, based on this original phantom, a series of testing data are generated by adding various levels of white noise, having standard deviation (SD) ranging from 5% to 80%. The noise SD is calculated as a percentage of the 8-bit dynamic range of the image (0–255). To our experience, the data with noise SD of 80% represents the most possibly challenging situation, which is well beyond any worst case of real angiography images. Fig. 10b–d present three samples of the testing data having noise SD of 5%, 45%, and 80%, respectively.

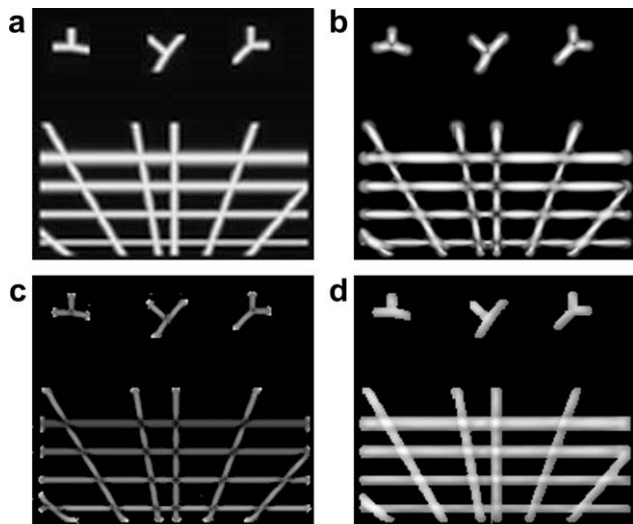


Fig. 9. Vessel enhancement results. (a) The original synthetic image. (b) Enhanced image by the Frangi method, cpu = 6.70 s, (c) by the Shikata method, 6.65 s, and (d) by our approach, 8.44 s. The Frangi and Shikata methods suppress the junctions while ours does not.

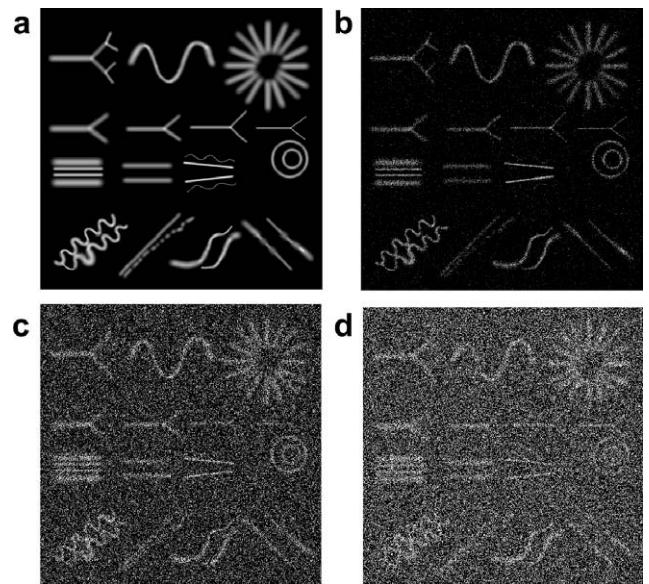


Fig. 10. Testing data with a size of 512×512 and different amount of white noise. (a) Original phantom (obtained from www.ecse.rpi.edu/censsis/phantom). (b) Noisy phantom with noise SD of 5%, (c) 45%, and (d) 80%. The testing data incorporate most of the common challenges to exact vessel extraction procedure such as image noise and presence of close parallel vessels, very thin vessels, discontinued vessels, and vessels with variable intensities along their length.

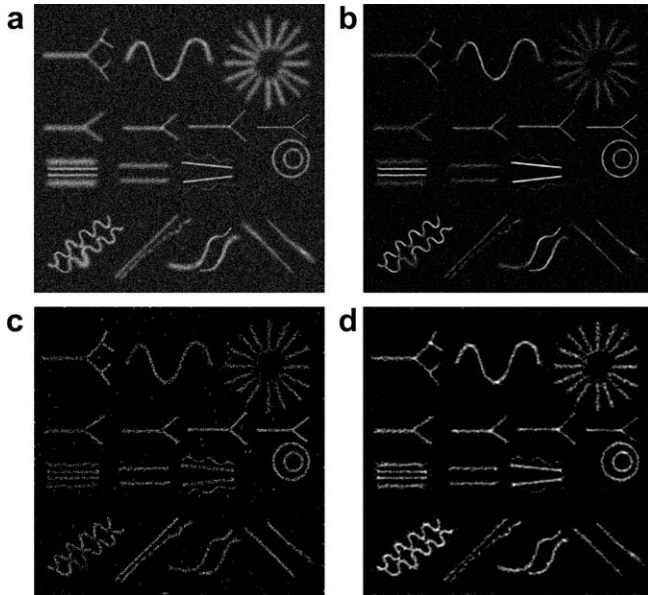


Fig. 11. Sample vessel enhancement results. (a) Sample phantom image with noise SD of 10%. (b) Enhanced image by the Frangi filter, cpu = 66.42 s, (c) by the Shikata filter, 65.86 s, and (d) by DFB-based filter, 81.27 s.

The three filters are then applied on those phantom images and the outputs are segmented using global thresholding to compare with the “ground truth”. The quantitative performance is measured with receiver operating characteristic (ROC) curves [45]. An ROC curve plots the rate of pixels correctly classified as vessels (i.e., true positive rate or *sensitivity*) against the rate of pixels incorrectly classified as vessels (i.e., false positive rate or $1 - \text{specificity}$). The rates are obtained with all possible threshold choices. Each discrete threshold value produces a (sensitivity, $1 - \text{specificity}$) pair corresponding to a single point in the curve. The closer the curve approaches the northwest corner, the better the filter performs. A single scalar value reflecting this behavior is the area under the ROC curve (AUC), which is 1 for perfect performance. Note that to get rid of the large number of background pixels correctly classified, one can compute the sensitivity and specificity in the vicinity of the “ground truth” vessels which can be obtained by dilation. In our experiment, the vicinity size is selected such that the number of background pixels is comparable to that of the vessel pixels.

Fig. 11 shows sample enhancement results for the data with noise SD of 10%. The performances of the three filters applied on the whole testing data set are presented in Fig. 12. In this figure, the AUC measures are plotted as a function of the noise SD. We can see that the DFB-based filter outperforms the others for this data set. Specifically, compared to the Frangi filter, it generates similar results in case of low noise (i.e., SD of 5–10%) but performs much better when the noise level increases.

4.3. Real data

Similar to junction suppression problem, small vessel enhancement is critical because those thin vessels which may appear broken or disconnected from larger structures will often be omitted in the reconstruction procedures. Fig. 13 shows the enhancement results of the three filters applied on two real angiography images. The images are of size 401×401 and belong to cardiac part of the human body. As can be observed, the Frangi filter gives good results with large vessels but fails to detect small ones while the Shikata model is able to enhance small vessels but unfortunately enhances background noise also. Conversely, the DFB-based filter can enhance small vessels with more continuous appearances.

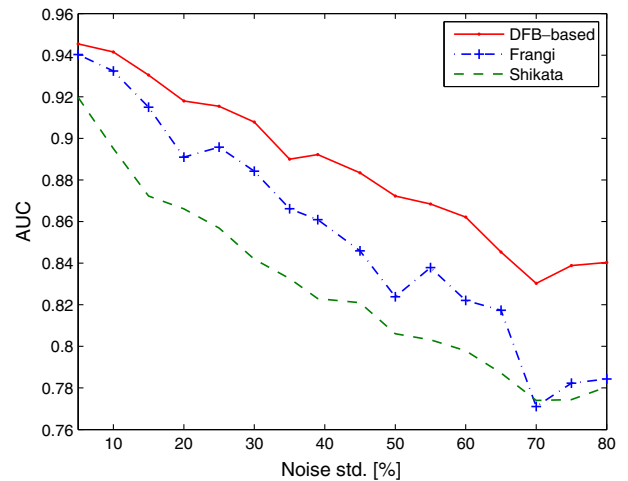


Fig. 12. Performance plots vs. noise levels for the testing data described in Fig. 10. In average, the AUC of DFB-based filter is relatively 3.74% and 7.02% larger than that of Frangi and Shikata filters, respectively.

Due to lack of ground truths for the above images, we leave them as qualitative results but instead utilize the Utrecht database¹ to quantitatively evaluate the three filters on real medical images. This database contains 40 retinal color images of size 584×565 and their corresponding vasculatures manually segmented by an expert, which are used as ground truths. In this experiment, the negative of the green channel of the image is used (see e.g., Fig. 14a and f). The green channel is selected since it gives the highest contrast and it is made negative because the filters assume that vessels are brighter than the background as stated in Section 2.4. Since vessels in these images are relatively small, the scale range $S = \{\sqrt{2}/2, 1, \sqrt{2}, 2, 2\sqrt{2}\}$ is used. The validation process is performed same as in Section 4.2.

Fig. 14 shows for the results with highest and lowest AUC measures. The performances of the three filters for the whole database are presented in Fig. 15 and the mean and standard deviation are given in Table 1.

To evaluate the noise sensitivity of the filters for retinal images, we create a testing data set similar to the previous section. Here, we use 40 ground truths of the Utrecht database as original phantom images; each is added with noise having SD ranging from 5% to 80%. By this way, we will have several images per noise level. Fig. 16 plots variation ranges of AUC per every noise level. Again, it can be seen that the DFB-based filter is least sensitive to noise among the three filters.

5. Discussions and conclusion

We have presented in this paper a novel approach of vessel enhancement for 2D angiography images by using directional decomposition. Our main contribution resides in adapting the Hessian-based filters to be used in the directional images. In particular, this permits the estimation of the vessel directions without the Hessian eigen-analysis. The advantage of the proposed approach is that it distinguishes all vessels at bifurcations and crossings. At these configurations, one will obtain different vessel directions and thus different second derivatives that are different from the Hessian eigenvalues (of the original image).

The larger the number of directional images n , the smaller the directional range and as a result the more accurate the eigenvalue estimation is, at the cost of the computation time. While the cpu time increases rather linearly with n , the performance does not in-

¹ Available at <http://www.isi.uu.nl/Research/Databases/DRIVE/>.

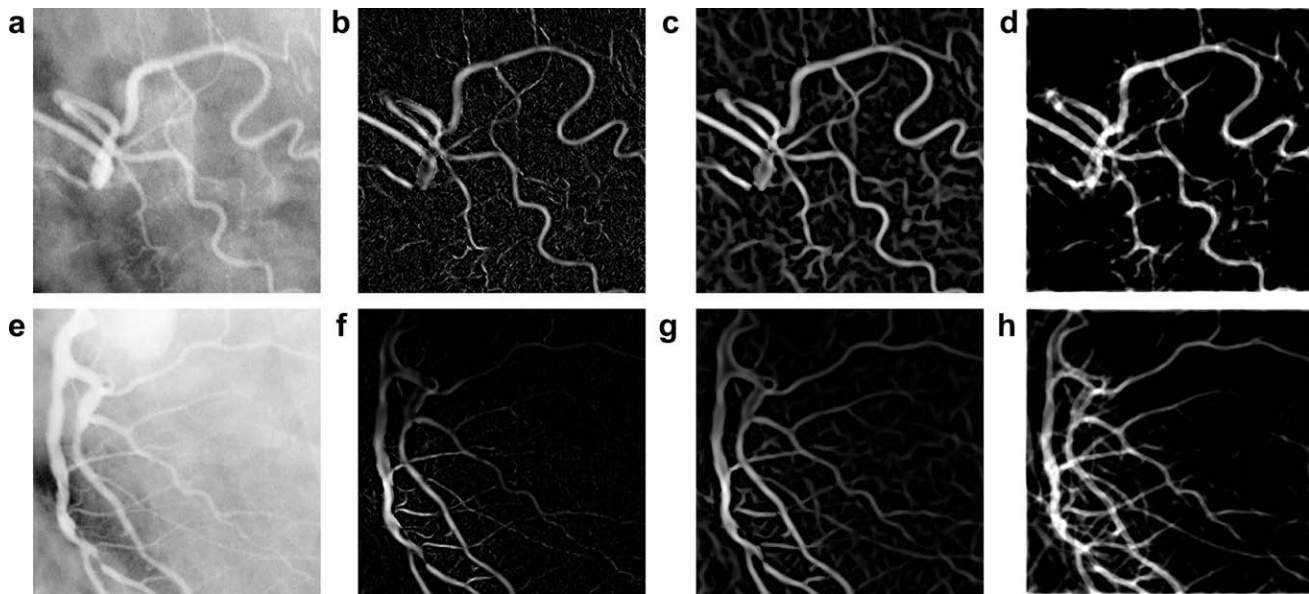


Fig. 13. Qualitative results for two cardiac angiography images. (a and e) Original images, (b and f) enhanced images by Frangi method, cpu = 43.22 s each, (c and g) by Shikata method, 43.11 s, and (d and h) by DFB-based approach, 49.08 s. The Frangi and Shikata models fail to correctly enhance small vessels but our approach succeeds.

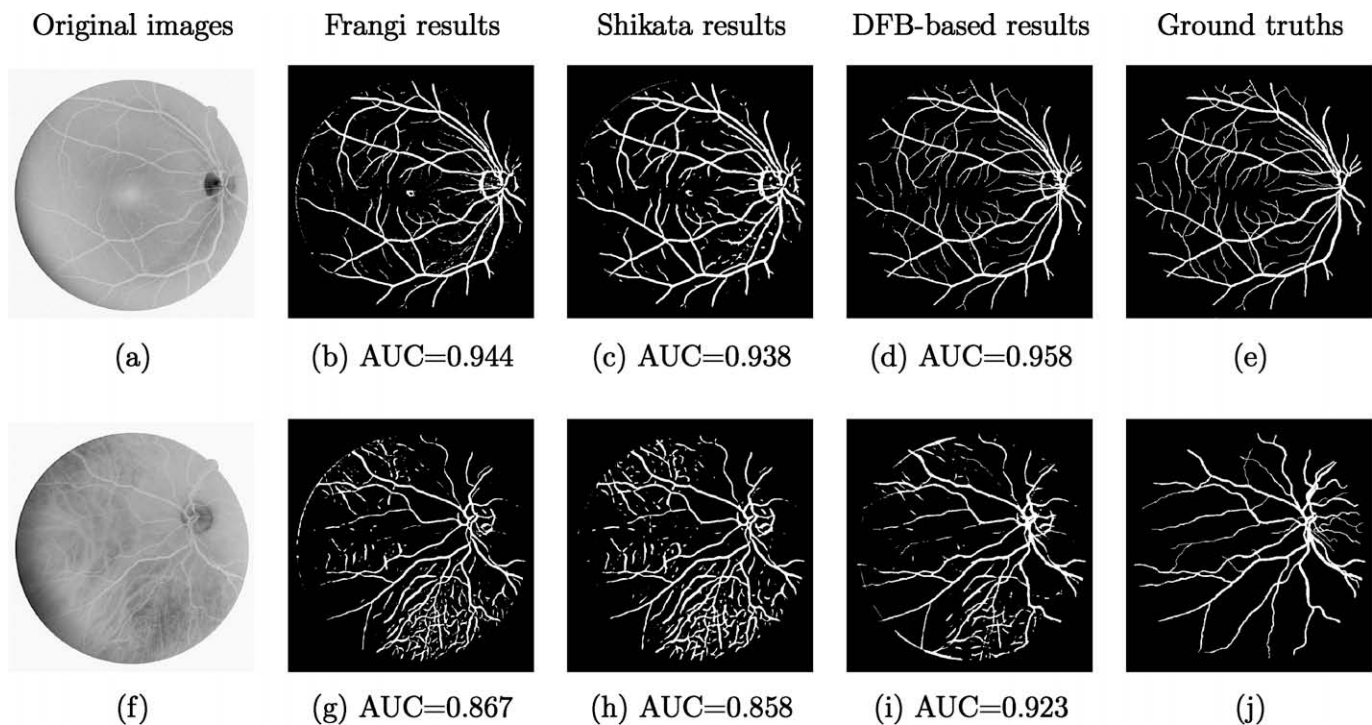


Fig. 14. Best and worst results for the Utrecht database in terms of AUC measures. For each image, the Frangi method cpu = 87.02 s, Shikata 85.55 s, and DFB-based 93.46 s.

crease as much. A pilot experiment showed that our filter with $n = 16$ performed about 4% better than that with $n = 8$ but the cpu time almost doubled. Also, it can be seen from the previous section that the cpu time of the DFB-based filter with $n = 16$ is comparable to those of the Frangi and Shikata filters (e.g., respectively, 93 s, 87 s, and 85 s for a retinal image of size 584×565). With those remarks, we use $n = 16$ rather than 32 or higher because the benefit on the relatively small performance gain is not worth the cost of much more computation time.

Another advantage of the DFB-based approach is the NUI removal using homomorphic filters on directional images. Looking at the dark disks in the retinal images in Fig. 14a and f, we can

see that the DFB-based filter can reduce these artifacts compared to the two other filters. Also, it has removed the bright blob at the center of the image in Fig. 14a whereas the others could not.

The experimental results show that the DFB-based filter overcomes the limitations of conventional Hessian-based methods such as junction suppression and noise sensitivity. It also performs better on real angiography images. In conclusion, we consider the proposed DFB-based filter a better candidate for pre-processing in an accurate vessel-tree reconstruction in clinical tasks.

Although in this work, we restrict ourselves to 2D images, the proposed approach can be extended to deal with 3D images by extending DDFB to 3D, which is our future work. The 2D-to-3D

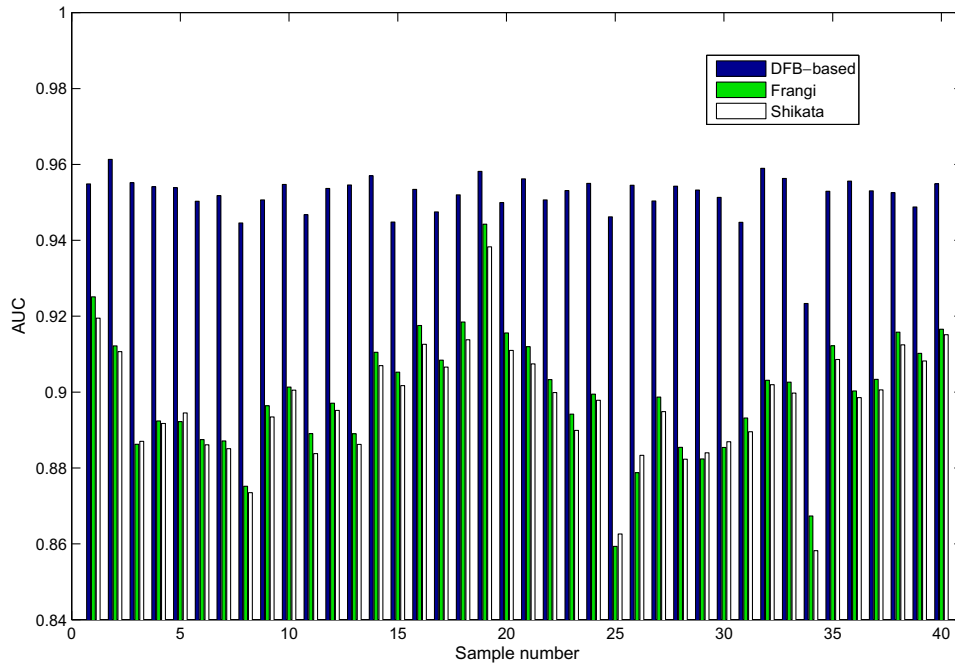


Fig. 15. Performance plots vs. sample number for the Utrecht database. The mean and SD of these measurements are given in Table 1. In average, the DFB-based filter is 5.8% and 6.2% better than the Frangi and the Shikata filters, respectively.

Table 1
Mean and SD of the AUC of the three methods performed on the Utrecht database

	Frangi	Shikata	DFB-based
Mean	0.8994	0.8970	0.9519
SD	0.0162	0.0152	0.0060

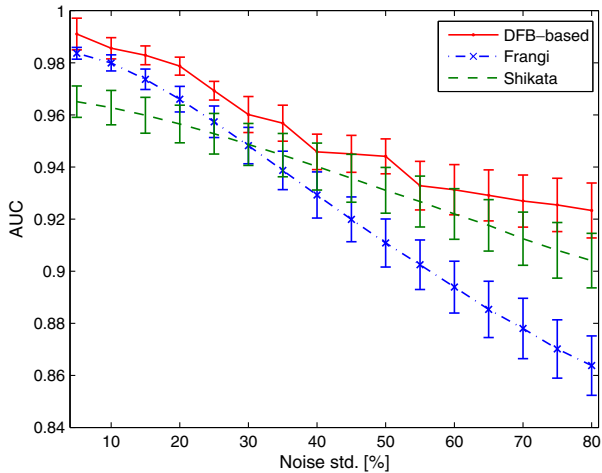


Fig. 16. Mean and SD bar plots of AUC vs. noise levels for 40 noise-added ground truths of the retinal images. In average, the AUC of DFB-based filter is relatively 3.47% and 2.36% larger than that of Frangi and Shikata filters, respectively.

DDFB extension can be done on the same lines as 2D DFB being converted to 3D DFB as described in [38]. Another aspect of future study will be on the clinical usage of the proposed technique.

Acknowledgments

This work was supported by grant (R01-2006-000-11209-0) from the Basic Research Program of the Korea Science and Engi-

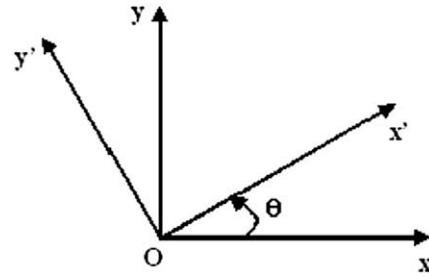


Fig. A-1. The coordinates Oxy is rotated to $Ox'y'$ by a counterclockwise angle θ .

neering Foundation. This research was supported by the MIC (Ministry of Information and Communication), Korea, under the ITRC (Information Technology Research Center) support program supervised by the IITA (Institute of Information Technology Advancement) (IITA-2006-(C1090- 0602-0002)).

This research was supported by the MIC, Korea, under the ITFSIP (IT Foreign Specialist Inviting Program) supervised by the IITA (C1012-0801-0003). This work was financially supported by the Ministry of Education and Human Resources Development (MOE), the Ministry of Commerce, Industry and Energy (MOCIE) and the Ministry of Labor (MOLAB) through the fostering project of the Lab of Excellency.

Appendix. Hessian matrix in new rotated coordinates

Given a function $f(x,y)$ in the coordinates Oxy . Suppose that:

- (1) Hessian matrix H of $f(x,y)$

$$H = \begin{bmatrix} \frac{\partial^2 f}{\partial x^2} & \frac{\partial^2 f}{\partial x \partial y} \\ \frac{\partial^2 f}{\partial x \partial y} & \frac{\partial^2 f}{\partial y^2} \end{bmatrix}$$

is known a priori.

- (2) The coordinates Oxy is rotated to $Ox'y'$ by an counterclockwise angle θ (see Fig. A-1).

Let us compute the Hessian matrix H' of f in $Ox'y'$

$$H' = \begin{bmatrix} \frac{\partial^2 f}{\partial x'^2} & \frac{\partial^2 f}{\partial x' \partial y'} \\ \frac{\partial^2 f}{\partial x' \partial y'} & \frac{\partial^2 f}{\partial y'^2} \end{bmatrix}.$$

We have

$$\begin{bmatrix} x \\ y \end{bmatrix} = \begin{bmatrix} \cos \theta & -\sin \theta \\ \sin \theta & \cos \theta \end{bmatrix} \begin{bmatrix} x' \\ y' \end{bmatrix} = \begin{bmatrix} x' \cos \theta - y' \sin \theta \\ x' \sin \theta + y' \cos \theta \end{bmatrix}.$$

Thus,

$$\frac{\partial f}{\partial x'} = \frac{\partial f}{\partial x} \frac{\partial x}{\partial x'} + \frac{\partial f}{\partial y} \frac{\partial y}{\partial x'} = \frac{\partial f}{\partial x} \cos \theta + \frac{\partial f}{\partial y} \sin \theta,$$

$$\frac{\partial f}{\partial y'} = \frac{\partial f}{\partial x} \frac{\partial x}{\partial y'} + \frac{\partial f}{\partial y} \frac{\partial y}{\partial y'} = \frac{\partial f}{\partial x} (-\sin \theta) + \frac{\partial f}{\partial y} \cos \theta.$$

Then

$$\begin{aligned} \frac{\partial^2 f}{\partial x'^2} &= \frac{\partial}{\partial x'} \left(\frac{\partial f}{\partial x'} \right) = \frac{\partial}{\partial x'} \left[\frac{\partial f}{\partial x} \cos \theta + \frac{\partial f}{\partial y} \sin \theta \right] \\ &= \cos \theta \left[\frac{\partial^2 f}{\partial x^2} \frac{\partial x}{\partial x'} + \frac{\partial^2 f}{\partial x \partial y} \frac{\partial y}{\partial x'} \right] + \sin \theta \left[\frac{\partial^2 f}{\partial y^2} \frac{\partial y}{\partial x'} + \frac{\partial^2 f}{\partial y \partial x} \frac{\partial x}{\partial x'} \right] \\ &= \frac{\partial^2 f}{\partial x^2} \cos^2 \theta + \frac{\partial^2 f}{\partial x \partial y} \sin (2\theta) + \frac{\partial^2 f}{\partial y^2} \sin^2 \theta. \end{aligned} \quad (A-1)$$

Similarly,

$$\frac{\partial^2 f}{\partial y'^2} = \frac{\partial^2 f}{\partial x^2} \sin^2 \theta - \frac{\partial^2 f}{\partial x \partial y} \sin (2\theta) + \frac{\partial^2 f}{\partial y^2} \cos^2 \theta, \quad (A-2)$$

and

$$\begin{aligned} \frac{\partial^2 f}{\partial x' \partial y'} &= \frac{\partial}{\partial x'} \left(\frac{\partial f}{\partial y'} \right) = \frac{\partial}{\partial x'} \left[\frac{\partial f}{\partial x} (-\sin \theta) + \frac{\partial f}{\partial y} \cos \theta \right] \\ &= -\sin \theta \left[\frac{\partial^2 f}{\partial x^2} \frac{\partial x}{\partial x'} + \frac{\partial^2 f}{\partial x \partial y} \frac{\partial y}{\partial x'} \right] + \cos \theta \left[\frac{\partial^2 f}{\partial y^2} \frac{\partial y}{\partial x'} + \frac{\partial^2 f}{\partial y \partial x} \frac{\partial x}{\partial x'} \right] \\ &= -\frac{1}{2} \frac{\partial^2 f}{\partial x^2} \sin (2\theta) + \frac{\partial^2 f}{\partial x \partial y} \cos (2\theta) + \frac{1}{2} \frac{\partial^2 f}{\partial y^2} \sin (2\theta). \end{aligned} \quad (A-3)$$

References

- [1] North American Symptomatic Carotid Endarterectomy Trial (NASCET) Steering Committee, North American symptomatic carotid endarterectomy trial, *Stroke* 22 (1991) 711–720.
- [2] European Carotid Surgery Trialists Collaborative Group, Randomised trial of endarterectomy for recently symptomatic carotid stenosis: final results of the MRC European Carotid Surgery (ECST), *Lancet* 351 (1999) 1379–87.
- [3] E.M. Haacke, R.W. Brown, M.R. Thompson, R. Venkatesan, *Magnetic Resonance Imaging: Physical Principles and Sequence Design*, Wiley, New York, 1999.
- [4] L. Lorigo, O. Faugeras, W. Grimson, R. Keriven, R. Kikinis, C.-F. Nabavi, C.-F. Westin, CURVES: curve evolution for vessel segmentation, *Med. Image Anal.* 5 (2001) 195–206.
- [5] C. Kirbas, F. Quek, A review of vessel extraction techniques and algorithms, *ACM Comput. Surv.* 36 (2) (2004) 81–121.
- [6] R. Poli, G. Valli, An algorithm for real-time vessel enhancement and detection, *Comput. Meth. Prog. Biomed.* 52 (1996) 1–22.
- [7] M. Wilkinson, M. Westenberg, Shape preserving filament enhancement filtering, in: *Proc. Int. Conf. on Medical Image Computing and Computer-Assisted Intervention*, LNCS, vol. 2208, Utrecht, The Netherlands, 2001, pp. 770–777.
- [8] S. Eiho, Y. Qian, Detection of coronary artery tree using morphological operator, in: *IEEE Comput. Cardiol.*, 1997, pp. 525–528.
- [9] F. Zana, J.-C. Klein, Segmentation of vessel-like patterns using mathematical morphology and curvature evaluation, *IEEE Trans. Imag. Proc.* 10 (2001) 1010–1019.
- [10] C. Yan, S. Hirano, Y. Hata, Extraction of blood vessel in CT angiography image aided by fuzzy logic, in: *IEEE Proc. Int. Conf. Signal Processing*, 2000, pp. 926–929.
- [11] K. Krissian, G. Malandain, N. Ayache, Directional anisotropic diffusion applied to segmentation of vessels in 3D images, in: *Scale-Space Theory in Computer Vision*, LNCS, 1997, pp. 345–348.
- [12] K. Krissian, Flux-based anisotropic diffusion applied to enhancement of 3-D angiogram, *IEEE Trans. Med. Imag.* 21 (11) (2002) 1440–1442.
- [13] M. Orkisz, C. Bresson, I. Magnin, O. Champin, P. Douek, Improved vessel visualization in MR angiography by nonlinear anisotropic filtering, *MRM* 37 (6) (1997) 914–919.
- [14] R. Czerwinski, D. Jones, W. O'Brien, Jr., An approach to boundary detection in ultrasound imaging, in: *Proc. IEEE Ultrasonics Symposium*, 1993, pp. 951–955.
- [15] R. Czerwinski, D. Jones, W. O'Brien Jr., Detection of lines and boundaries in speckle images-application to medical ultrasound, *IEEE Trans. Med. Imag.* 18 (2) (1999) 126–136.
- [16] R. Kutka, S. Stier, Extraction of line properties based on direction fields, *IEEE Trans. Med. Imag.* 15 (1) (1996) 51–58.
- [17] H. Chen, J. Hale, An algorithm for MR angiography image enhancement, *MRM* 33 (4) (1995) 534–540.
- [18] Y.P. Du, D.L. Parker, W.L. Davis, Vessel enhancement filtering in three-dimensional MR angiography, *JMRI* 5 (3) (1995) 353–359.
- [19] Y.P. Du, D.L. Parker, Vessel enhancement filtering in three-dimensional MR angiograms using long-range signal correlation, *JMRI* 7 (2) (1997) 447–450.
- [20] A. Frangi, W. Niessen, K. Vincken, M. Viergever, Multiscale vessel enhancement filtering, in: *Medical Image Computing Computer-Assisted Intervention*, LNCS, vol. 1496, 1998, pp. 130–137.
- [21] A. Frangi, W. Niessen, R. Hoogeveen, T. van Walsum, M. Viergever, Model-based quantitation of 3-D magnetic resonance angiographic images, *IEEE Trans. Med. Imag.* 18 (10) (1999) 946–956.
- [22] A. Frangi, W. Niessen, P. Nederkoorn, J. Bakker, W. Mali, M. Viergever, Quantitative analysis of vascular morphology from 3D MR angiograms: in vitro and in vivo results, *MRM* 45 (2001) 311–322.
- [23] Y. Sato, S. Nakajima, N. Shiraga, H. Atsumi, S. Yoshida, T. Koller, G. Gerig, R. Kikinis, Three-dimensional multi-scale line filter for segmentation and visualization of curvilinear structures in medical images, *Med. Image Anal.* 2 (2) (1998) 143–168.
- [24] C. Lorenz, I.-C. Carlsen, T. Buzug, C. Fassnacht, J. Weese, A multi-scale line filter with automatic scale selection based on the Hessian matrix for medical image segmentation, in: *Proc. Scale-Space Theories in Computer Vision*, LNCS, vol. 1252, 1997, pp. 152–163.
- [25] H. Shikata, E.A. Hoffman, M. Sonka, Automated segmentation of pulmonary vascular tree from 3D CT images, in: *Proc. SPIE Int. Symp. Medical Imaging*, vol. 5369, San Diego, CA, 2004, pp. 107–116.
- [26] K. Krissian, G. Malandain, N. Ayache, R. Vaillant, Y. Troussset, Model-based detection of tubular structures in 3D images, *Comput. Vis. Image Und.* 80 (2) (2000) 130–171.
- [27] G. Agam, I.S.G. Armato, C. Wu, Vessel tree reconstruction in thoracic CT scans with application to nodule detection, *IEEE Trans. Med. Imag.* 24 (4) (2005) 486–499.
- [28] G. Bamberger, M.J.T. Smith, A filter bank for the directional decomposition of images—theory and design, *IEEE Trans. Signal Process.* 40 (4) (1992) 882–893.
- [29] R.H. Bamberger, New subband decompositions and coders for image and video compression, in: *IEEE Int. Conf. on Acoustics, Speech and Signal Processing*, vol. 3, 1992, pp. 217–220.
- [30] S. Park, M.J.T. Smith, J.J. Lee, Fingerprint enhancement based on the directional filter bank, in: *IEEE Int. Conf. on Image Processing (ICIP'00)*, 2000, pp. 793–796.
- [31] R.H. Bamberger, New results on two and three dimensional directional filter banks, in: *IEEE Twenty-Seventh Asilomar Conference on Signals, Systems and Computers*, vol. 2, 1993, pp. 1286–1290.
- [32] C.H. Park, J.J. Lee, M.J.T. Smith, S. Park, K.J. Park, Directional filter bank-based fingerprint feature extraction and matching, *IEEE Trans. Circ. Syst. Video Technol.* 14 (1) (2004) 74–85.
- [33] S. Park, M.J.T. Smith, R.M. Mersereau, A new directional filter bank for image analysis and classification, *ICASSP* 3 (1999) 1417–1420.
- [34] S. Park, M.J.T. Smith, R.M. Mersereau, Improved structures of maximally decimated directional filter banks for spatial image analysis, *IEEE Trans. Image Process.* 13 (11) (2004) 1424–1431.
- [35] R.H. Bamberger, *The Directional Filter Bank: A Multirate Filterbank for the Directional Decomposition of Images*, Ph.D. thesis, Georgia Institute of Technology, USA, November, 1990.
- [36] R.H. Bamberger, M.J.T. Smith, A multirate filter bank based approach to the detection and enhancement of linear features in images, in: *IEEE Int. Conf. Acoustics, Speech and Signal Processing (ICASSP'91)*, vol. 4, 1991, pp. 2557–2560.
- [37] B.L. Evans, R.H. Bamberger, J.H. McCellan, Rules for multidimensional multirate structures, *IEEE Trans. Signal Process.* 42 (4) (1994) 762–771.
- [38] S. Park, *New Directional Filter Banks and their Applications in Image Processing*, Ph.D. thesis, Georgia Institute of Technology, USA, November, 1999.
- [39] F. Mujica, R. Murenzi, J.-P. Leduc, M.J.T. Smith, Robust object tracking in compressed image sequences, *SPIE J. Electron. Imag.* 7 (1998) 746–754.
- [40] F. Mujica, J.-P. Leduc, R. Murenzi, M.J.T. Smith, Spatio-temporal continuous wavelets applied to missile warhead detection and tracking, in: *Proc. SPIE Visual Communication and Image Processing*, vol. 3024, 1997, pp. 787–798.
- [41] L. Florack, B. Romeny, J. Koenderink, M. Viergever, Scale and the differential structure of images, *Image Vision Comput.* 10 (6) (1992) 376–388.
- [42] T. Lindeberg, *Scale-Space Theory in Computer Vision*, Kluwer Academic, Dordrecht, The Netherlands, 1994.
- [43] T. Lindeberg, Edge detection and ridge detection with automatic scale selection, in: *IEEE Conf. on Computer Vision and Pattern Recognition (CVPR)*, San Francisco, 1996, pp. 465–470.
- [44] R. Gonzalez, R. Woods, *Digital Image Processing*, Prentice Hall, New Jersey, USA, 2002.
- [45] T. Fawcett, *ROC Graphs: Notes and Practical Considerations for Researchers*, Technical Report, HP Laboratories, Palo Alto, USA, 2004.